ULTRASONIC TESTING OF RAILS INCLUDING VERTICAL CRACKS - NUMERICAL MODELING AND EXPERIMENTAL RESULTS

F. Schubert, B. Koehler
Fraunhofer-IZFP, Branch Lab EADQ
Kruegerstrasse 22
D-01326 Dresden (Germany)

O. Sacharova
Railway University
St.Petersburg (Russia)

INTRODUCTION

One of the possible reasons for the failure of rails in railway tracks is the appearance of vertical cracks in the head, neck or bottom of the rail (see Fig. 1). Therefore, it is necessary to detect such defects at an early stage when the cracks are still of smaller dimensions. For vertical cracks, results of ultrasonic pulse-echo measurements are difficult to interpret due to mode conversions at the crack and rail surfaces, respectively. For normal incidence, not only the attenuation of the primary wavefront but also new echoes due to converted wave modes can be observed in the A-scan data.

In the present paper, ultrasonic testing of rails with vertical cracks is investigated experimentally and by numerical simulations. For this purpose, four different rail specimens were used. An ideal rail without any crack and three specimens with vertical cracks artificially generated in the head, neck and bottom of the rail. Additionally, wave propagation in the cross-section of the rail was modeled numerically by using a special version of EFIT (Elastodynamic Finite Integration Technique) that was optimized for the given testing conditions.

EXPERIMENTAL SETUP

The experimental measurements were carried out by using a multifunctional flaw detector (USIP-12, Krautkraemer-Branson). Normal piezoelectric longitudinal and shear wave transducers (Panametrics V154) having a circular aperture with a diameter of 12.7 mm were coupled at the center of the top surface of the rail head. They were used in pulse-echo configuration with a center frequency of 2.25 MHz . The A-scan-HF data were stored using a digital oscilloscope.

Review of Progress in Quantitative Nondestructive Evaluation, Vol. 18
Edited by Thompson and Chimenti, Kluwer Academic/Plenum Publishers, 1999

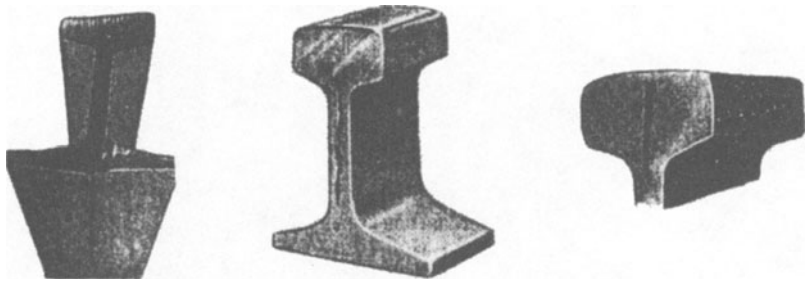

Figure 1. Pictures showing rails with real cracks at the bottom (left), the neck (center) and the head of the rail (right).

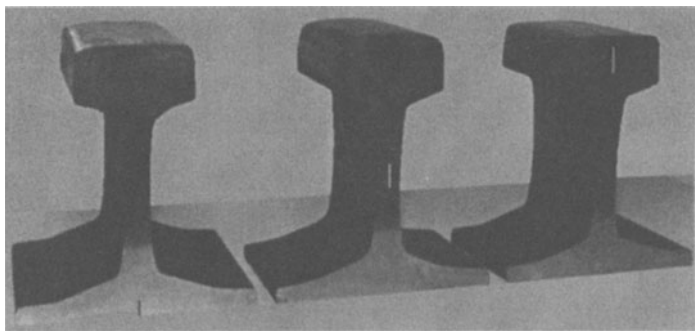

Figure 2. Specimens used in the measurements. The model cracks were produced artificially by spark machining.

THE SPECIMENS

Figure 2 shows three of the four specimens used in the measurements. The height was 169 mm in each case, the width at the rail bottom 154 mm. The cracks were generated artificially by spark machining with a crack width of less than 0.3 mm. The specimens in detail:

1. Rail without any cracks (no figure).
2. Rail with a vertical non-surface breaking 18 mm crack in the head of the rail, starting in 7 mm depth under the top surface (Fig. 2, right).
3. Rail with a vertical 15 mm crack in the middle of the rail neck (Fig. 2, center).
4. Rail with a vertical surface breaking 10 mm crack at the bottom of the rail (Fig. 2, left).

NUMERICAL SIMULATIONS

The simulation of wave propagation in the different rails was carried out by using a special version of EFIT (Elastodynamic Finite Integration Technique) which was originally developed by Fellinger et al. [1]. The FIT discretization of the integral form of the basic equations of linear elasticity, Hooke's law and the equation of motion, leads to very stable and efficient numerical code of second order accuracy which is applicable to a wide range of NDT problems [2-4]. For reasons of computer capacity, in most cases only two-dimensional simulations are practicable representing a 'plane strain' propagation process. Due to this limitation , we realized two-dimensional artificial rail models representing the

cross-sections of the real specimens. In this paper, only shear waves polarized in the plane of the rail's cross-section were investigated.

The cracks and the outer rail surfaces were modeled as stress-free boundaries. Since the cross-sectional testing geometry was symmetric to the vertical axis of the rail, the simulations were carried out in only one half of the rail by by using appropriate boundary conditions at the axis. For a better presentation, both parts of the rail are shown in the following wavefront snapshots. These snapshots were taken at different times representing the absolute value of the particle displacement velocity vector. Additionally, pulse-echo HF-A-scans were detected by averaging the signal over all discrete grid points inside the transducer aperture.

The base material of the rails was stainless steel with the acoustic properties ρ = 7800 kg/m³, c_P = 5900 m/s and c_S = 3250 m/s. Longitudinal and shear wave transducers with normal incidence were used emitting an RC2-pulse with a center frequency of 2.25 MHz. The width of the aperture line (2D-model !) was 12.7 mm. The spatial discretization of the quadratic grid was $\Delta x = \Delta y$ = 71.7 µm (53.8 µm), the temporal discretization Δt = 7.8 ns (6.3 ns), where the values in paranthesis were used for the simulations with the shear wave transducer. The number of effective grid cells amounted to 765 000 (1 354 000) while the number of time steps was 10 260 (20 600) due to a total observation time of about 80 µs (130 µs). The crack width was modeled by 5 grid cells leading to a width of about 0.3 mm.

RESULTS

In the following sections, ultrasonic wave propagation in the different specimens is discussed in detail by comparing the experimental measurements with the results of the numerical simulations.

Ideal Rail without Cracks

Figure 3 shows EFIT time snapshots of the wave propagation in the ideal rail without cracks. The P-wave transducer was located centrally on the rail head. The snapshots are in a good agreement with experimental Schlieren examinations by Hall done at glass model rails [5].

The primary wavefront propagating through the neck of the rail is reflected at the rail bottom and runs back to the transducer where it can be detected about 58 µs after signal input. In the rail neck, so called secondary ultrasonic echoes are generated due to mode conversions at the rail boundaries (see Fig. 4, left). The transformation sequence is: Primary P-wave ⇒ Head/shear-waves ⇒ Secondary P-waves ⇒ Secondary US echo.

The distance between the different secondary echoes and their amplitudes are mainly influenced by the width an the geometry of the rail neck. In this case, the first secondary echo arrives at 62 µs, the second one at 67 µs. Fig. 5 shows both, measured and modeled HF-A-scans for the given testing situation. They are in a good agreement to each other. There are only small differences in the pulse form due to the fact, that the input signals used in the simulations were slightly different from those in the measurements.

For the shear wave, no significant mode conversion at the rail neck boundaries can be observed (Fig. 4, right) and therefore secondary echoes are not generated.

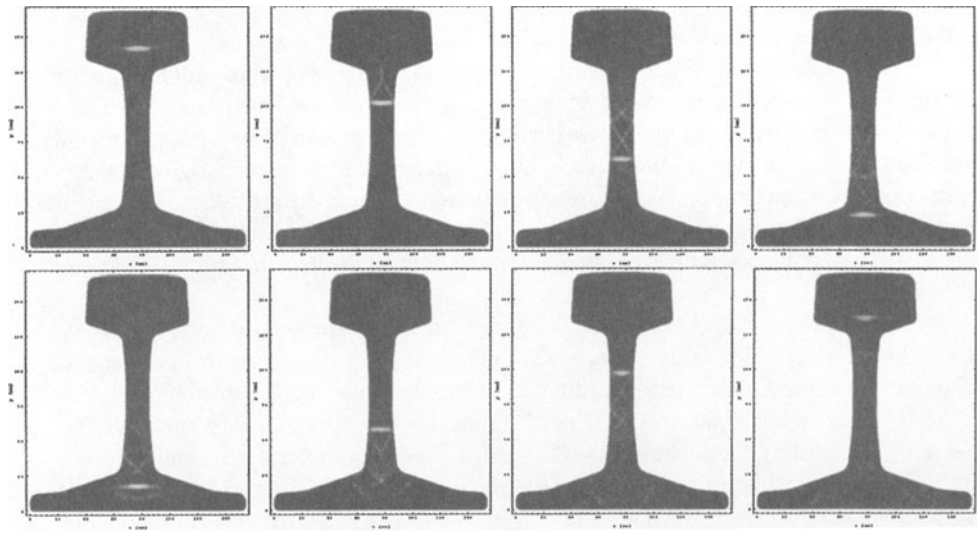

Figure 3. EFIT time snapshots of wave propagation in the rail without cracks (P-wave transducer placed centrally on the rail head)

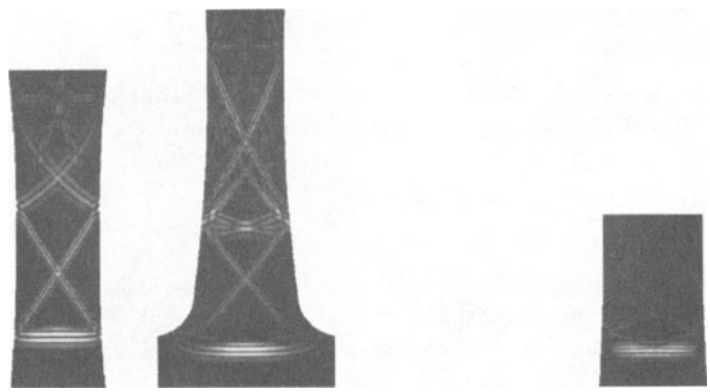

Figure 4. Detailed representation of elastic wave interaction with the rail neck boundaries in an ideal rail without cracks (left side: P-wave transducer, right side: S-wave transducer).

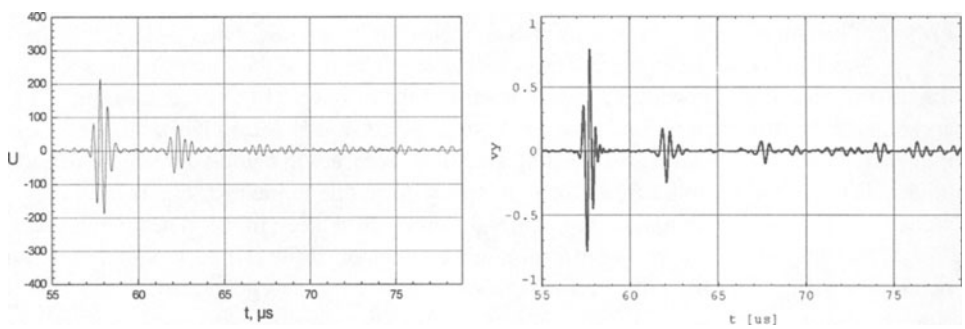

Figure 5. P-wave A-scan of the ideal rail specimen showing bottom echo and secondary ultrasonic echoes (left side: measured, right side: EFIT modeling).

Rail with Vertical Crack in the Rail Head

Figure 6 shows wavefront snapshots in the rail specimen with a vertical crack in the rail head. The P-wave mode conversions at the crack (Fig. 7, left) produce two significant head-waves running sideways into the head of the rail. Moreover, a Rayleigh wave is generated immediately at the crack surface [6].

The head-waves are reflected at the rail head boundaries and turn back to the transducer, where a new echo can be detected at about 31 μs (see Fig. 8). Additionally, one can observe different crack tip echoes produced by the primary wavefront and the Rayleigh wave. Again there is a good qualitative agreement between experiment and simulation but there are quantitative differences in the relative amplitudes of the different echoes. This is obviously caused by the fact that the simulations were two-dimensional (i.e. strip-like transducer aperture in the direction of the longitudinal rail axis) while the measurements were three-dimensional (circular transducer aperture). Another fact that cannot be excluded is, that the modeled cross-section was slightly different from the cross-section of the real specimen. Furthermore, there were some inaccuracies in the measurements due to unstable coupling conditions.

Because of the mode conversions described above, the bottom echo and the following secondary echoes are significantly attenuated in comparison to the case of an ideal rail without cracks (this is not shown in the A-scan section in Fig. 8). This statement is also true for the shear wave propagation, where no head-waves but also Rayleigh waves are generated (Fig. 7, right) and therefore, only the annenuated bottom echo can be observed in the corresponding A-scan (no figure).

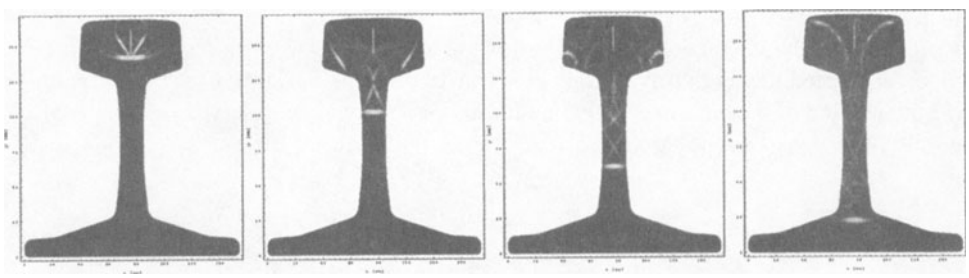

Figure 6. EFIT time snapshots of wave propagation in the rail with vertical crack in the rail head (P-wave transducer).

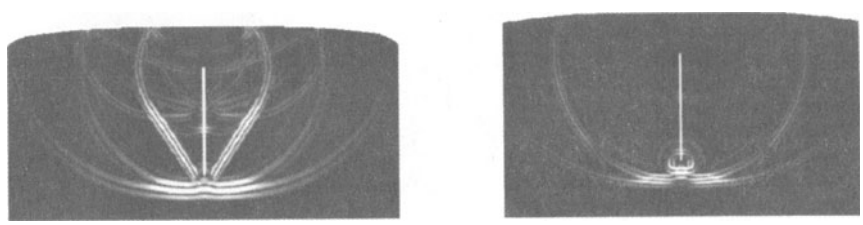

Figure 7. Detailed representation of elastic wave interaction with a crack in the rail head (left side: P-wave transducer, right side: S-wave transducer).

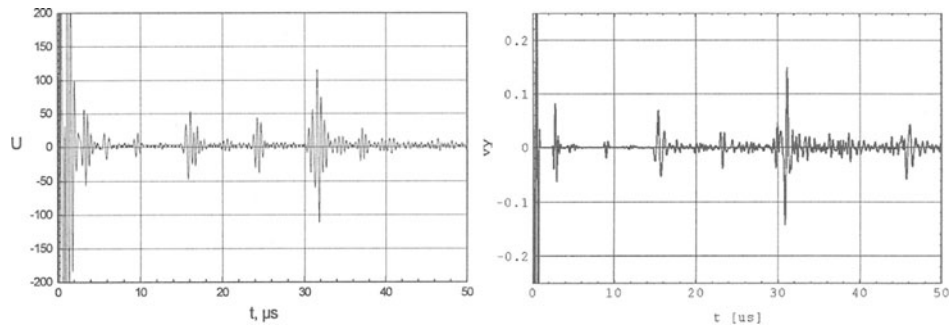

Figure 8. P-wave A-scan of the rail with crack in the head, showing crack tip echoes and the head-wave reflex (left side: measured, right side: EFIT modeling).

Rail with Vertical Crack in the Rail Neck

Figure 9 (left) shows EFIT time snapshots of the P-wave propagation in the rail with a vertical crack in the rail neck. The crack bisects this rail region into two parts with only half the width of the original neck. Therefore, a new secondary echo is generated directly between the bottom echo and the former first secondary echo (see Figs. 9+10). Again, the agreement between experiment and simulation is qualitatively good with differences in the relative amplitudes. It should be mentioned that the rail specimen used in this case was somewhat different from those in the other measurements (compare Fig. 2). In particular, the vertical dimension of the rail head was bigger so that all echoes arrived about 1 µs later than in the other cases.

Again, the interaction between a shear wavefront and the crack only produces a mode-converted Rayleigh wave but no head-waves (see Fig. 9, right). Consequently, only the attenuation of the bottom echo but no further reflexes can be observed in the corresponding A-scan (no figure).

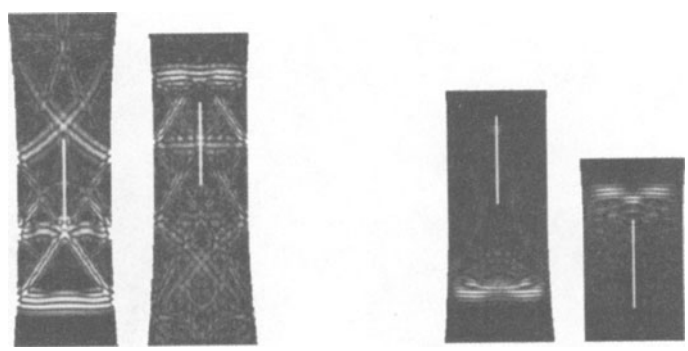

Figure 9. Detailed representation of elastic wave interaction with a crack in the rail neck (left side: P-wave transducer, right side: S-wave transducer, in each case downward and upward propagation).

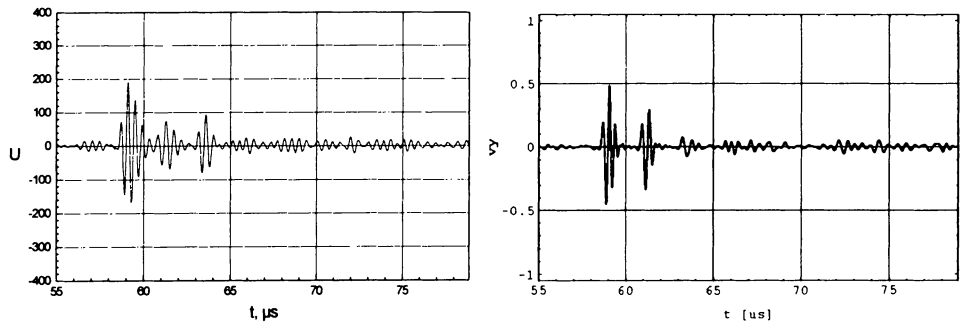

Figure 10. P-wave A-scan of the rail with crack in the neck, showing the new secondary echo between the (attenuated) bottom echo and the former first secondary echo (left side: measured, right side: EFIT modeling).

Rail with Vertical Surface-Breaking Crack at the Bottom of the Rail

Figure 11 shows EFIT snapshots of P-wave propagation in the specimen with a surface-breaking crack at the bottom of the rail. Similar to the case in which the crack was located in the rail head, two significant head-waves are generated (Fig. 12, left). They run sideways into the rail bottom and therefore they cannot be detected by the transducer located on the rail head. Consequently, only the attenuation of the bottom echo and the following secondary echoes can be observed in the A-scans (Fig. 13). The arrival times of the different echoes in simulation and experiment are nearly identical but the attenuation of the signals in the EFIT calculation is less significant than in the measurement (see Fig. 5).

The interaction between the shear wave and the bottom crack produces two strong Rayleigh waves running outwards along the bottom surface (Fig. 12, right). Hence, in the corresponding A-scan a significant attenuation of the bottom echo was observed and was found to be stronger than for the longitudinal wave (no figure).

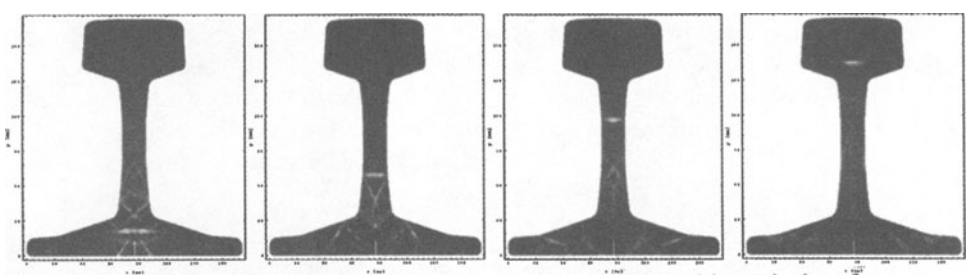

Figure 11. EFIT time snapshots of wave propagation in the rail with vertical surface-breaking crack at the rail bottom (P-wave transducer).

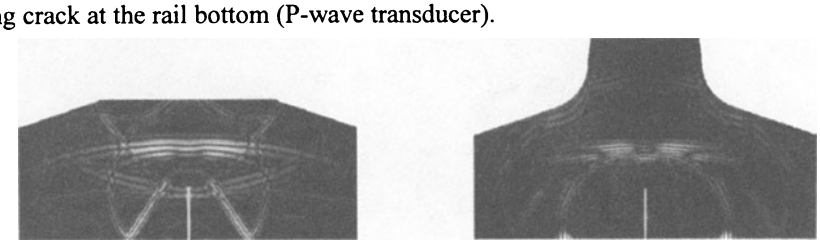

Figure 12. Detailed representation of elastic wave interaction with a crack at the rail bottom (left side: P-wave transducer, right side: S-wave transducer).

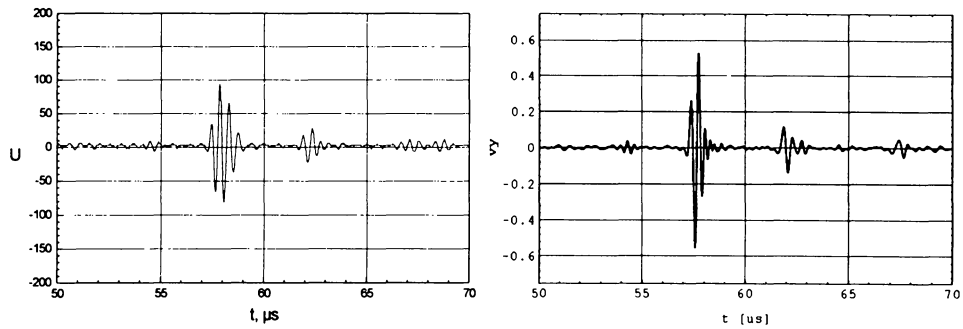

Figure 13. P-wave A-scan of the rail with crack at the bottom, showing attenuated bottom echo and secondary echoes (left side: measured, right side: EFIT modeling).

CONCLUSIONS

The good qualitative agreement between the measurements and the numerical simulations for the different testing situations shows the accuracy of the developed numerical code. By the help of the simulations, all mode conversions at the crack and rail surfaces were cleared up leading to a better understanding and interpretation of the received signals. A significant attenuation of the rail bottom echo for the three different crack locations were found for both, shear and longitudinal waves. The most important difference between the two wave modes is the fact that the interaction between primary shear wavefront and the crack or rail surfaces does not produce new echoes in the A-scan like head-waves or secondary echoes as described for the P-wave.

It should be mentioned that the method using piezoelectric shear wave transducers is unpracticable for fast testing of real rails in railway tracks due to coupling-problems. But this can be solved by using EMA-transducers.

Further investigations should involve more realistic crack geometries and various crack parameters such as width, length, depth, orientation, surface roughness and so on, different frequencies and moreover, shear waves with a polarization plane perpendicular to the rail cross-section. The latter problem can be treated with a special three-dimensional EFIT model that consists of only one grid cell in the direction of the longitudinal rail axis if a strip-like transducer is still taken as a basis. A broader future perspective of the investigations should involve a classification of typical rail defects in the pulse-echo mode of ultrasonic testing.

REFERENCES

1. P. Fellinger, R. Marklein, K. J. Langenberg and S. Klaholz, Wave Motion 21, 47 (1995).
2. R. Marklein, R. Baermann and K. J. Langenberg, in *Review of Progress in QNDE*, Vol. 14, eds. D. O. Thompson and D. E. Chimenti (Plenum, New York, 1995), p. 251.
3. F. Schubert and B. Koehler, in *Nondestructive Characterization of Materials VIII*, (Plenum, New York, 1998), p. 567.
4. F. Schubert and B. Koehler, "CEFIT - A numerical modeling tool for axisymmetric wave propagation in cylindrical media", these proceedings.
5. K. G. Hall, Materials Evaluation 42, 922 (1984).
6. V. P. Lochov, Defektoskopiya 3, 39 (1989).